

## Research paper

## A numerical study of pore formation mechanisms in aluminium cold spray coatings

Sebastien Weiller\*, Francesco Delloro

Mines ParisTech, PSL Research University, MAT - Centre des Materiaux, CNRS UMR 7633, BP 87, Evry, 91003, France



## ARTICLE INFO

**Keywords:**  
 Cold spray  
 Finite element  
 Porosity simulation  
 CEL

## ABSTRACT

Porosity is critical regarding cold sprayed coatings properties: it can be an asset for certain applications as in tribology, it is generally at the cost of mechanical and anti-corrosion properties. It is thus important to understand the mechanisms at its origin, in order to have a better control over it. Since the build-up process of a cold spray coating cannot be directly observed at a microscopic scale, numerical simulation is the only way to address the mechanisms of pore formation. The main purpose of this study is to understand by dedicated simulations the mechanisms, acting during the build-up of a cold spray coating, giving rise to pore formation mechanisms. Besides, an user-independent method developed to assess porosity from these simulations is presented. The first part of the study, analysing the results of a 500 particles impact simulation, shows that porosity is mainly caused by two intricate mechanisms: interfacial porosity is created by a geometrical effect at particle/particle interfaces, whereas stack porosity is caused by particle density variations in the gas flow. Then, an original method, based on the commutation of successive convex hulls, to estimate porosity from multi-particle impact simulations is presented. Initial particles position has a strong influence on this estimation and the reference volume to compute porosity must therefore be thoroughly chosen. Finally, porosity computed by numerical simulation are compared to 3D X-ray microtomography measurements.

## 1. Introduction

Cold spray is a thermal spray process relying on the acceleration of solid powder particles by a pressurized gas, typically air,  $N$  or He. Particles are injected into a convergent-divergent “De Laval” nozzle, in which they are accelerated to supersonic speeds [1]. The build-up of a cold spray coating can be seen as an iterative process where each elementary event, *i.e.* the impact, deformation and adhesion of a single particle, is repeated millions of times. From an experimental point of view, the mechanisms behind coating build-up and those responsible for pore formation are not observable with present day techniques. Only recent works allowed to observe single particle impacts at cold spray velocities [2] and powder distribution within the gas flow stream outside the nozzle [3]. Numerical simulation is therefore necessary to investigate phenomena related to coating build-up, happening at the micrometre/microsecond scale.

The present work aims at highlighting the mechanisms involved in pore formation in cold sprayed coatings, with the use of Finite Element Analysis (FEA). It would be out of the scope of the present work to review all the numerical methods deployed for the simulation of the cold spray process. Nevertheless, a brief, non-exhaustive review concerning particle impact and coating build-up modelling is important

to draw up the state of the art around the main topics of the present article.

Different FEA formulations were discussed in the review article of [4]: pure Lagrangian [5–8], Arbitrary Lagrangian Eulerian (ALE) [9–11], pure Eulerian [12] and Coupled Eulerian Lagrangian (CEL) [13, 14]. FEA-alternative methods can also be considered, as for example Smoothed Particle Hydrodynamics (SPH) [15]. The pure Lagrangian approach is affected by heavy element distortions, causing convergence problems and lack of accuracy. Hybrid methods, as ALE, can mitigate this drawback [16], although the solution becomes dependent on remeshing parameters. The CEL method finally seems the most appropriate for large deformation regimes as those found in cold spray, due to its robustness and its lower computational cost when compared to pure Eulerian methods, as discussed in [17] and in the review by Fardan et al. [18]. Another kind of approach, recovering data from FEA and using them for the coating build-up simulation with a large number of particles, was proposed in [9].

Several studies deal with the modelling of single particle impacts. Even if the deformation behaviour of isolated particles must be understood and validated to ensure FEA accuracy, this approach is not

\* Corresponding author.

E-mail address: [sebastien.weiller@mines-paris.org](mailto:sebastien.weiller@mines-paris.org) (S. Weiller).

representative of coating build-up mechanisms, involving particle interactions, and variability on their sizes, and speeds. A notable exception is the study of cases where particles possess a complex internal structure, as for example the agglomerated powders studied in [19]. Here, the deformation behaviour of single particles is already difficult to model and is a necessary step before moving further to coating build-up simulations.

More macroscopic approaches can be found in literature, aiming to simulate the coating build-up at a larger scale. They are achieved without considering particles, and limiting themselves to material addition, and thermal considerations on the model of what is done in other additive processes, as for example [20,21]. This approach, at the scale of the part, lacks detailed description of the particular microstructure of cold sprayed materials. This is due to the granular nature of the process.

Multi-particle impact models lies in between the microscopic approach of single-particle simulations and the macroscopic one of homogeneous material deposition. The interest of these methods is to take into account the elementary events of the cold spray process (*i.e.* particle impacts), allowing to study complex particle interactions, not accessible when limiting to a single particle impact. In some papers, authors oversimplify the variability of the process, assuming for example particles as perfect spheres, all with the same size and arranged on a regular grid as in [22]. An approach closer to reality is proposed by Terrone et al. [23] where multi-particle multi-material simulations were performed to predict the microstructure of porous structures, obtained by the removal of the sacrificial component in the as-sprayed composite by means of chemical etching. In the modelling part of the work, a systematic FE scheme based on the CEL approach was developed and applied to the cold spraying of Ti-Al and Ti-Cu feedstock powder mixtures. The inputs are the number of particles for one constituent phase and the corresponding volume percentage in the feedstock powder. Then, the model randomly positions each particle in the empty space inside the Eulerian domain, while avoiding any overlap. The algorithm assigns velocity and temperature fields, correlated to individual particle diameters according to the fitted equation from KSS model output. Simulations contained about 600 Ti particles and the corresponding required number of Cu ones. The focus of this work was the prediction of coating porosity after the removal of the sacrificial phase and did not discuss collective particle behaviour bringing to the formation of porosity in the deposited material.

Song et al. [13] developed multi-particle CEL impact simulations with the aim of studying porosity formation. Instead of focusing on the mechanisms at the origin of porosity, the authors studied the effect of temperature and particle velocity on porosity. In conclusion, substrate temperature did not affect the coating porosity level significantly, which was controlled by particle temperature and velocity. Here, porosity was measured from simulations using a sampling cuboid. This method has two major drawbacks: (i) it is user-dependent and (ii) it is potentially not representative of the whole coating. Aside from these studies focused on simulating porosity in cold spray coatings, the literature addresses porosity from the experimental point view, characterizing coatings by cross-sectional SEM (Scanning Electron Microscope) image analyses [5,24] or X-ray microtomography (XMT) [25].

In the present study, a FEA CEL based model, implemented in the commercial software Abaqus/Explicit v6.14, was used to investigate pore formation mechanisms in cold spray coatings by simulating multi-particle impacts. The CEL method was chosen among the cited methods for this complex task because of its robustness, lacking in classical Lagrangian methods [13,17]. The quantification of porosity in simulations was performed by an original user-independent method developed in the present work, namely the Successive Convex Hulls (SCH) method. The modelling approach was validated against 3D experimental observations, by X-ray Micro-Tomography (XMT in the following), of aluminium and aluminium-alumina cold sprayed coatings. These experimental results were obtained in a previous work of the authors [26], where a deep analysis of the XMT images is presented.

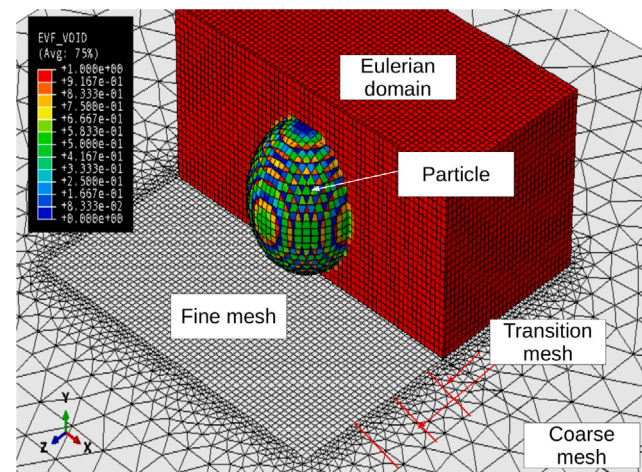


Fig. 1. Meshing of the Eulerian and Lagrangian domains, with  $mf = 0.1$ .

## 2. Materials and methods

### 2.1. Modelling methods

The CEL finite element method was chosen for the simulations. This choice have been made because of its superior robustness for multi-particle impact simulations in regards to the Lagrangian or ALE methods [18]. The Eulerian domain was a cuboid, in which particles were placed using the Abaqus Volume Fraction Tool. The algorithm creates a discrete field by tracking the intersection of each particle with the Eulerian grid. In this way, a void value (from 0 to 1) is assigned to each element. Elements were 8 nodes hexahedra with thermo-mechanical coupling and reduced integration, called EC3D8RT in Abaqus.

Mesh size can be described introducing a mesh factor ( $mf$  in the following), defined as a function of the radius of the smallest particle in the domain, as follows:

$$m = mf \min_{Part \in \Omega_{Part}} R(Part) \quad (1)$$

where  $m$  is the mesh size,  $mf$  the mesh factor,  $R(Part)$  particle radius and  $\Omega_{Part}$  the set of all particles in the simulation. For instance, if the smallest particle radius is  $10 \mu\text{m}$ , the mesh size will be  $1 \mu\text{m}$  if the mesh factor is chosen as 0.1. Given that example, each particle in the simulation will contain at least  $\approx 4188$  elements, i.e.  $\frac{4\pi}{3} \left(\frac{1}{mf}\right)^3$ . The mesh factor is therefore a convenient tool to monitor mesh size without needing to make computations regarding particle size.

To fit to the experimental configuration, the substrate was modelled as a A2017-T4 aluminium alloy. It was described as a Lagrangian part, as proposed by [13,14]. It was divided into three domains with different mesh sizes. The part intersecting with the Eulerian domain has the finest mesh. It is regular grid with the same element size as the eulerian domain. Element type is C3D8RT thermo-mechanical. A transition zone and a coarsely meshed zone were placed, to limit computational cost. These consisted in tetrahedral C3D4T thermo-mechanical elements. Fig. 1 illustrates the meshing of the Eulerian and Lagrangian domains, with a mesh factor of 0.1 and a single particle.

#### 2.1.1. Material model

Both particles and substrate were assumed to obey the visco-plastic Johnson–Cook (JC) material behaviour model [27]. The semi-empirical Johnson–Cook model is widely used in cold spray impact simulations [8]. It relates the flow stress  $\sigma$  of a material to its strain rate,

its equivalent plastic strain and its absolute temperature:

$$\sigma = (A + Be^n)(1 + C\ln(\frac{\dot{\epsilon}}{\dot{\epsilon}_0}))(1 - T^{*m})$$

$$T^* = \begin{cases} 0 & \text{si } T < T_0 \\ \frac{T-T_0}{T_f-T_0} & \text{si } T_0 \leq T \leq T_f \\ 1 & \text{si } T_f \leq T \end{cases} \quad (2)$$

With:

- A the yield stress (MPa);
- B and n the linear (MPa) and non linear (-) hardening stresses;
- C The strain sensitive coefficient (-);
- $\epsilon$ ,  $\dot{\epsilon}$  and  $\dot{\epsilon}_0$  the equivalent plastic strain, the plastic strain rate ( $s^{-1}$ ) and a reference plastic strain rate;
- $T_0$ ,  $T_f$  and m, a reference temperature (K), the melting temperature (K) and the thermal softening coefficient (-).

This model is completed with an Us-Up Mie–Grüneisen equation of state [28] and a shear modulus. The Mie–Grüneisen equation of state relates several thermodynamic quantities together, accounting for the elastic behaviour of the material when a shock wave passes through it. It is assumed that the response of the material is adiabatic and that the velocity of the shock wave is related to the velocity of a particle by the following relationship:

$$U_s = c_0 + sU_p \quad (3)$$

With  $U_s$  and  $U_p$  the velocities of the shock and the particle,  $c_0$  the speed of sound in the material and  $s$  the slope of the experimentally determined relation. Then, the Mie–Grüneisen equation of state yields :

$$p = \frac{\rho_0 c_0^2 \eta}{(1 - s\eta)^2} \left(1 - \frac{\Gamma_0 \eta}{2\rho_0}\right) + \Gamma_0 \rho_0 E \quad (4)$$

With p the internal pressure (Pa),  $\rho_0$  ( $kg\ m^{-3}$ ) the density of the material in reference state,  $c_0$  ( $m\ s^{-1}$ ) the speed of sound in the material,  $s$  (-) a material constant,  $\eta = 1 - \frac{\rho}{\rho_0}$ ,  $\rho$  being the current density,  $\Gamma_0$  (-) a material constant and E the internal energy per unit reference mass ( $J\ kg^{-3}$ ).

Materials parameters are summed up in Table 1. The JC was chosen because it is already implemented and numerically optimized in Abaqus, despite other model being proposed by [29] or [30]. The adoption of another material behaviour model would have implied to use a VUMAT subroutine, resulting in much longer computational times which would have been a major problem in the realization of the present work. Simulations results in the present work were used to qualitatively understand and illustrate basic mechanisms of porosity formation. Material behaviour at the particle scale can be assumed to have little influence on the qualitative analysis at the coating scale: with several dozens of particles impacting at the same time, The single behaviour of a particle is hidden in the collection of impacts.

Two types of simulations were carried out:

- Single-impact simulations for the mesh size.
- Multi-particle impact simulations, to highlight the mechanisms involved in the creation of porosity and to compare simulated microstructures with real coatings.

The simulation to highlight pore formation mechanisms was carried out with 500 particles of pure aluminium, following a grain size distribution detailed later 2.2.2. Other multi-particle impact simulations were carried out to assess porosity level and compare them to experimental observations. These were including 100 particles, with only aluminium or aluminium and alumina. In the latter case, 85 out of the 100 particles were made of aluminium, and 15 of alumina, in order to account for the aluminium/alumina blend used for experimental spraying (20% wt.).

A conventional nomenclature is introduced describing relevant details of each simulation:  $T$  the initial temperature (K),  $V$  the initial

**Table 1**  
Material parameters for aluminium and Al 2017 alloy.

Quantity	Aluminium	Al 2017
Thermo-mechanical parameters		
Mass density $\rho$ ( $kg\ m^{-3}$ )	2700	2700
Shear modulus G (GPa)	26.4	26.4
Thermal conductivity $\lambda$ ( $W\ m^{-1}K^{-1}$ )	229	229
Heat capacity $C_p$ ( $J\ K^{-1}kg^{-1}$ )	889	889
Johnson–Cook	Aluminium, from [31]	Al 2017, from [32]
A (MPa)	110	279.2
B (MPa)	150	398
n (-)	0.36	0.198
C (-)	0.014	-0.0138
$\dot{\epsilon}$ (-)	1	0.01
m (-)	1	1.2619
$T_0$ (K)	293	293
$T_m$ (K)	931	943
Mie–Grüneisen	Aluminium from [33]	Al 2017, from [32]
$c_0$ ( $m\ s^{-1}$ )	5300	5386
s (-)	1.34	1.34
$\Gamma_0$ (-)	2.16	2.09

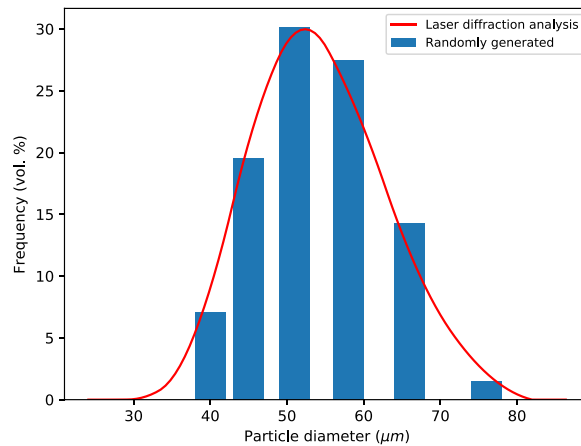


**Fig. 2.** Comparison of particle size distributions: experimental (curve) and generated for the simulation (histogram).

velocity ( $m\ s^{-1}$ ) and  $Al_2O_3$  index. The latter is 0 in the absence of alumina particles and 1 in the case of 15 alumina particles.

For instance, 500 particles  $T$  412  $V$  550  $Al_2O_3$  0 yields “simulation with 500 particles at initial temperature of 412 K, initial speed of 550  $m\ s^{-1}$  and no alumina”.

### 2.1.2. Particle generation

Particle sizes were generated according to the grain size distribution of the feed-stock powder measured by a Masterizer 3000©from MALVERN (United Kingdom). Fig. 2 compares the experimental particle size distribution, with those generated by the algorithm (the bar histogram), in a case with 100 particles.

Particles were then positioned within the Eulerian domain following three rules: non-intersection, minimum distance to avoid particles being stuck and maximal distance, preventing particles to be too far away from each other. Mathematical expression of these conditions is presented in Appendix A. A given set of n-randomly generated particles following the above algorithm will be called “configuration” in the following. Fig. 3 shows 500 particles in a given configuration.

Particle initial speeds and temperatures were estimated by a 1D isentropic gas flow model, proposed by Champagne et al. [34]. The model needs as inputs gas and material properties, gas stagnation temperature, and pressure, and geometrical parameters (nozzle sections and stand-off distance). Fig. 4 shows the speed and temperature of a

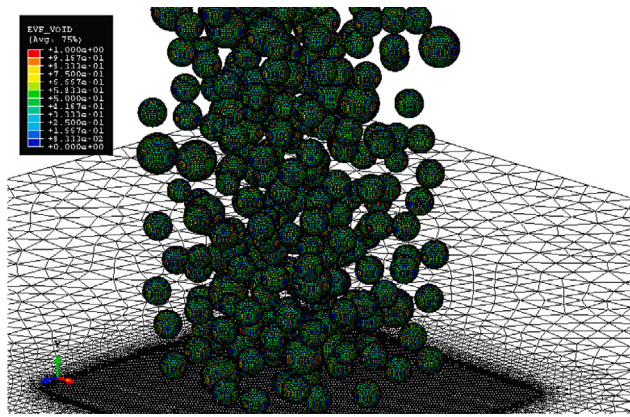


**Fig. 3.** Initial state of a multi-particle impact simulation, showing a configuration with 500 particles.

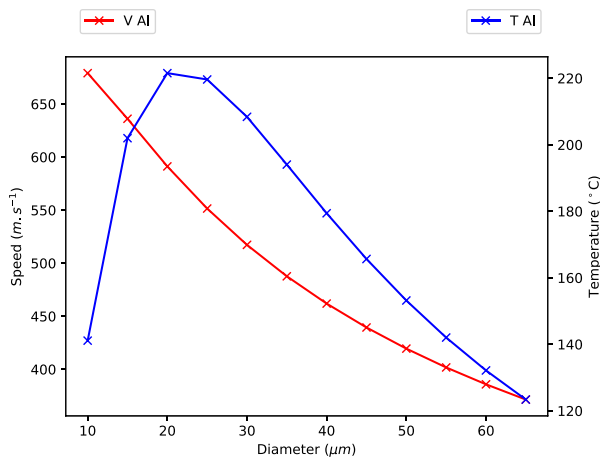


**Fig. 4.** Impact speed and temperature of an aluminium particle as a function of its diameter, computed with a 1D isentropic gas flow model.

**Table 2**  
Table of initial conditions for single particle simulations.

Mesh factor	Radius ( $\mu\text{m}$ )	Velocity ( $\text{m s}^{-1}$ )	Temperature (K)
0.5, 0.2, 0.1	5, 10, 20, 30	500, 600, 700, 800	373, 473, 573

spherical aluminium particle as a function of its diameter, as predicted by the isentropic model with the above-mentioned parameters for a 30 mm stand-off distance, a nitrogen carrier gas at 3 MPa, 300 °C and the PBI nozzle. Nozzle geometry and spraying parameters are detailed in 2.4.

## 2.2. Modelling hypothesis

### 2.2.1. Single particle impact

Single particle impact simulations were performed to determine an optimal mesh factor, resulting from the compromise between computational time and accuracy. The following fields have been extracted from the simulations for a particle in the deformed state :average and maximum temperature ;average and maximum PEEQ; flattening ratio of the particle, as defined in [35],  $\tau_f = \frac{2r-h}{2r}$ , with r the radius of the particle before impact and h its height after impact.

In Abaqus, PEEQ stands for the equivalent plastic deformation. Table 2 summarizes the parameters used for the simulations. All possible combinations were simulated.

Simulations were carried out on 3 cores Intel(R) Xeon(R) Gold 5118 CPUs running at 2.3 GHz. Their duration was a few dozen of seconds for a mf of 0.5 and about 20 min for a mf of 0.1.

### 2.2.2. Multi-particle impact

A population of 500 particles was chosen to assess pore formation mechanisms. Its radius size distribution and frequency was as follows:  $r \in \{10, 12, 17\} \mu\text{m}$ , with a frequency of, respectively, 0.1, 0.8 and 0.1, which means that 10% of the particles have a 10  $\mu\text{m}$  radius and so on. Particles were generated in a cuboid of size [0.19, 0.19, 0.72] mm  $\text{m}^3$ . Initial speed and temperature were supposed to be common to all particles, namely 412 K and 550  $\text{m s}^{-1}$ . This simplification was made to reduce computational time and to assess mechanisms involved in pore formation with a reduced number of variables: only three classes of particle size, all with the same initial temperature and velocity.

The choice of the mesh factor was based on the results of the mesh size study on single particle simulations and will be given in the “Results and Discussions” section. The computational time for such a simulation was about 500 h when carried out on a 35-cores Intel(R) Xeon(R) Gold 5118 CPUs, running at 2.3 GHz.

For the assessment of porosity level, alumina was also included in the simulations. The alumina oxide layer on the aluminium particles was not modelled. Particle sizes were assigned according to experimental measurements of powder size distributions. Initial temperature and speed of particles were computed with the 1D CFD model presented above. For these reasons, only 100 particles were chosen for the simulations: a greater number of particles would have led to a disproportionately high computational time regarding the purposes of this study. Numerically computed porosity levels were compared with XMT observations made on cold sprayed samples. Details about methods used to assess porosity by XMT are given in [26].

### 2.3. The successive convex hulls (SCH) method

The evaluation of porosity level in simulation results is based on the choice of a sampling volume in which it can be measured. The choice of this sampling volume is therefore crucial to estimate the porosity as accurately as possible. However, in previous works found in literature, the choice of this volume depends on the user: it is often chosen to be cube shaped and located at the heart of the cluster of deposited particles [13], even with more sophisticated methods [23]. Estimation errors can then occur, either because the volume considered is too small, or because it is chosen in a zone that is more or less dense in pores. A method based on the calculation of successive convex hulls has been developed to avoid the above-mentioned problems. The main advantage of the method, besides being user-independent, is that it maximizes the sample volume based on the actual geometry of the simulated coating. The convex hulls were computed with the Python ConvexHull sub-library available in the `scipy.spatial` library. It is based on the algorithm of Chan [36] for the calculation in 3 dimensions.

The algorithm on which SCH method relies can be described as follows, given  $A$  a set of points.

- (1) Define a stop criterion  $0 < w < 1$ .
- (2) Compute the convex envelope  $E_{c,A}$  of  $A$ . Let us call  $S_{E_{c,A}}$  its vertices.
- (3) Define a subset  $A_i$  of  $A$ , containing all the points of  $A$  except those constituting the vertices of the envelope  $E_{c,A}$ .  $A_i = A - S_{E_{c,A}}$
- (4) Repeat step 2 on  $A_i$  until the cardinal  $\text{Card}A_i \leq w\text{Card}A$ ,  $w$  being the stop criterion for the sequence (for example 1%, as chosen in the present work).

A set of successive convex hulls (SCH)  $E_{c,A_i}$  is obtained in such a way, strictly included one in the other:  $E_{c,A_n} \subset E_{c,A_{n-1}} \dots \subset E_{c,A}$ . It is not interesting to go below a minimum number of points, as the volume becomes too small to be representative.

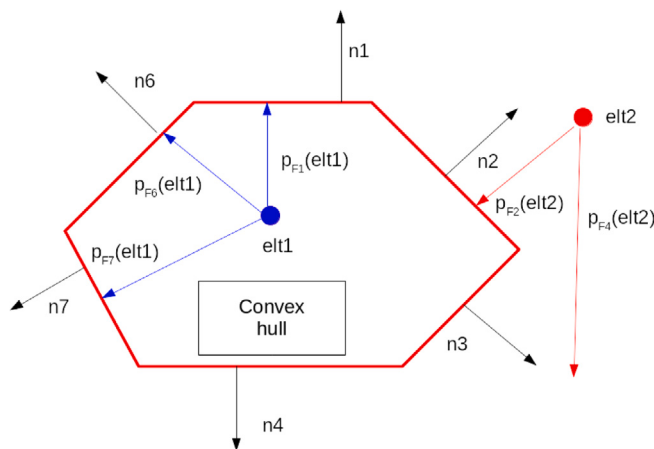


Fig. 5. Schematic example in 2D for testing if a point belongs to a convex hull.

The SCH method was then applied to the set of nodes belonging to elements containing at least 95% of matter.

In order to compute porosity in a given convex hulls, one should first determine the elements belonging to that set. To know if an element  $elt$  lies within a convex envelope  $E_c$ , the following test can be performed:

- Define  $F = \cup F_i$  the set of faces  $F_i$  of  $E_c$ , and  $\vec{n}_i$  the vector normal to  $F_i$  coming out of  $E_c$ .
- Compute the orthogonal projection of the barycentre of  $elt$  on  $F_i$  and name its unit vector  $\vec{p}_{F_i}(elt)$ .
- If, for each  $F_i$ , the scalar product  $\vec{n}_i \cdot \vec{p}_{F_i}(elt) \geq 0$ , then  $elt$  lies within  $E_c$ , otherwise it is outside.

Fig. 5 illustrates the test through a simple 2D example. The point  $elt1$  is inside the convex hull: the scalar product of each of the director vectors of its orthogonal projections on the faces with the outgoing normals is positive or zero. The point  $elt2$  is outside:  $\vec{n}_2 \cdot \vec{p}_{F_2}(elt) < 0$ .

The pore volume fraction  $p$  inside a given convex envelope  $E_c$  was calculated as follows:

$$p_i = \frac{1}{N} \sum_{j=1}^N v_j \quad (5)$$

with  $N$  the number of elements in the convex hull and  $v_j$  the volume fraction of void in the element  $j$ .

#### 2.4. Powders, cold spray facility and XMT

The feed-stock powder used in the present work was a commercial 1070 aluminium, produced by Toyo Aluminium (Osaka, Japan) and with [40, 72]  $\mu\text{m}$  particle size. This powder was chosen because particles were almost perfect spheres. Fig. 6(a) shows a SEM-BSE (Scanning Electron Microscope — Back Scattered Electrons) top view of the powder. This is very convenient for the comparison of impact simulations with experimental results. Some coatings were made using as feed-stock powder a blend of the spherical aluminium with 20% wt. spherical alumina, produced by Saint-Gobain (Cavaillon, France). It was obtained by plasma spheroidization of an angular alumina powder and had [10, 26]  $\mu\text{m}$  particle size. Fig. 6(b) shows a SEM-BSE top view of the powder. Some angular particles can be observed, probably leftovers of the spheroidization, the yield of the process not being 100%. Open porosity is visible on some particles, while others were hollow or fractured. Fig. 7 shows the grain size distribution of the aluminium and alumina powders.

Feed-stock powders were sprayed onto 3 mm thick square substrates (30 mm long), made of aluminium alloy A2017-T4 and cut from a

laminated plate. No particular surface treatment was applied before spraying. All coatings were produced by a Kinetics 3000 cold spray system, from CGT, now owned by Oerlikon Metco (Kelsterbach, Germany), with nitrogen as principal gas.

Two different cold spray nozzles, manufactured by Oerlikon Metco (Kelsterbach, Germany), were used for the spraying.

- A polymer nozzle, denoted 33PBI, composed of polybenzimidazole (PBI,  $(\text{C}_{20}\text{H}_{12}\text{N}_4)_n$ ), was used for spraying pure aluminium. As alumina tends to erode the PBI, it was not used for spraying mixtures.
- A tungsten carbide nozzle, denoted 24TC, used for spraying mixtures Al +  $\text{Al}_2\text{O}_3$ . Its use for pure aluminium was not possible because of nozzle clogging issues.

The following process parameters (gas pressure and temperature) are used:

- For the 24TC nozzle geometry: 3 MPa 300 °C, 3 MPa 400 °C and 2.5 MPa 350 °C with aluminium-alumina 20% wt. blend.
- For the 33PBI nozzle 3 MPa and 300 °C and pure aluminium.

XMT observations were led at the Soleil synchrotron, at CEA (Commissariat à l'énergie atomique et aux énergies alternatives, Gif-Sur-Yvette, France) on the ANATOMIX (Advanced Nanotomography and Imaging with coherent X rays) beam-line. A cuboid sample of  $500 \times 500 \times 500 \mu\text{m}^3$  was cut from the coating, near the substrate-coating interface. The beam was monochromatic at 20 keV and the spatial resolution was 0.325  $\mu\text{m}$  per voxel. Fig. 8 shows a 2D slice from the 3D image. Image size is  $1380 \times 1488 \times 500$  voxels ( $448 \times 483 \times 162 \mu\text{m}^3$ ).

The images were treated with the SMIL (Simple Morphological Image Library) Python Library, developed by M. Faessel [37]. Details about images treatment is given in [26].

## 3. Results and discussion

### 3.1. Single particle impact simulations

Single particle impact simulations were carried out for mesh study purposes. The mesh factor chosen will then be used for multi-particle impact simulations. Computational times on 4 cores are 15 mn, a few minutes and a few dozen of seconds for  $mf = 0.1, 0.2$  and  $0.5$  respectively.

We will refer to the quantity “deviation”, for a given field  $C$  (mean and max PEEQ, mean and max temperature, and flattening ratio), between  $mf = 0.1$  (the finer mesh size is considered as a reference for these comparisons) and  $mf = x$  at given radius (5, 10, 20 or 30  $\mu\text{m}$ , see 2) as follows:

$$e_{mf=x,C} = 1 - \frac{1}{n_{T_{ini}} n_{V_{ini}}} \sum_{i \in T_{ini}} \sum_{j \in V_{ini}} \left| \frac{C_{i,j,mf=x}}{C_{i,j,mf=0.1}} \right| \quad (6)$$

With  $x = 0.2$  or  $0.5$ ,  $T_{ini}$  and  $V_{ini}$  the set of initial temperatures and velocities, and  $n_{T_{ini}}$ ,  $n_{V_{ini}}$  their number. In this case, the product  $n_{T_{ini}} n_{V_{ini}} = 12$ . The closer the deviation  $e_{mf=x,C}$  is to 0, the more similar the values of the fields are.

With  $mf = 0.5$ , the fields are badly estimated whatever the radius, with deviations  $\geq 20\%$ , going up to  $\geq 50\%$  for PEEQ.

Results given by  $mf = 0.2$  were closer to the reference. Deviations for average and maximum temperature were in the range 7–11.5%. PEEQ was better estimated as well, but still revealed deviations between 20 and 40%. Nevertheless, the flattening ratio was well estimated, with a maximum average deviation of 5.5%.

These differences can be explained by the fact that for a coarser mesh, the fields are averaged in a larger volume in the impact area. In the case of a finer mesh, the fields are computed in smaller volumes and localized in the impact area.

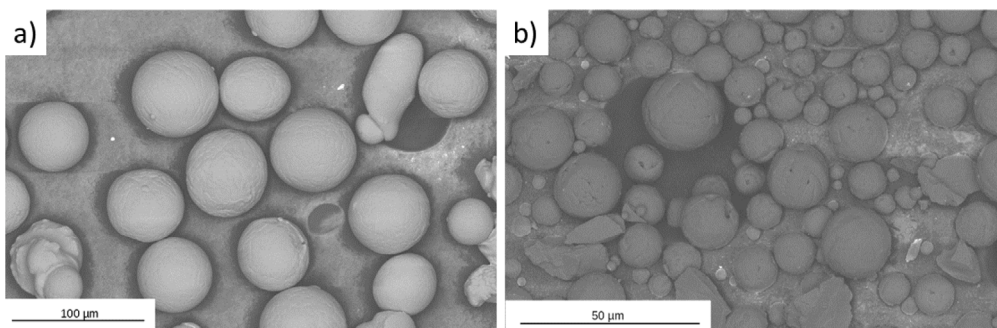


**Fig. 6.** SEM-BSE top view image of the aluminium powder (a), the alumina powder (b).

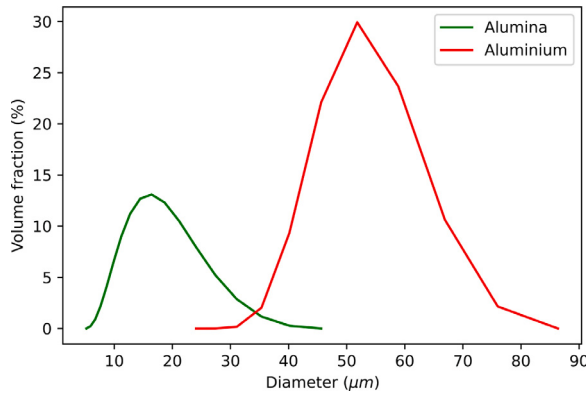


**Fig. 7.** Grain size distribution of the aluminium and alumina powders.

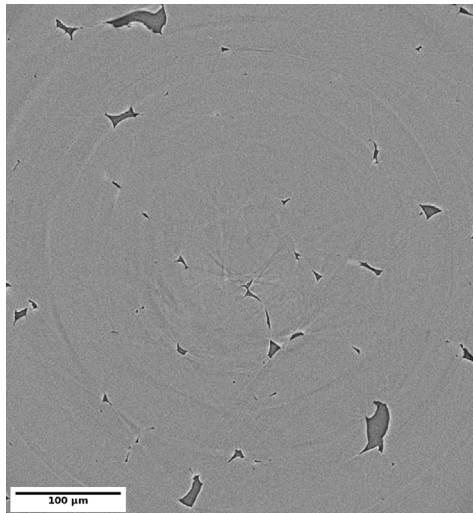


**Fig. 8.** XMT slice of the coating sprayed with the ultra-spherical powder at 300 °C and 3 MPa.

CEL modelling approach was capable of capturing the jetting phenomenon, consisting in the ejection of material at particle impact. In the simulations, its onset depended on particle velocity and temperature, and on the mesh size, in accordance with [38]. For  $mf = 0.1$ , it showed up for an initial temperature of 573 K. For 473 K it showed up for initial velocities  $\geq 700 \text{ m s}^{-1}$ . Jetting was also present in the case  $mf = 0.2$ , but only for  $T_{ini} = 573 \text{ K}$  and  $V_{ini} \leq 700 \text{ m s}^{-1}$ .

Fig. 9 shows some single particle simulation results, with and without jetting.

The better compromise between accuracy and computational cost was given by the intermediate mesh size, corresponding to  $mf = 0.2$ . It

allowed to limit computational time and to give a good estimation of the flattening ratio. The latter is an important feature when studying coating build-up and porosity formation mechanisms.

Single particle impact simulations allowed to conclude on the choice of an optimal mesh size for the rest of the work. In the context of this study, a mesh factor between 0.2 and 0.1 was considered as the best compromise between accuracy and calculation time. It will therefore be set at  $\frac{1}{6} \cong 0.15$  for all the forthcoming simulations.

### 3.2. Multi-particle impact simulations

#### 3.2.1. Pore formation mechanisms

The formation of the coating is tracked over time in order to highlight the mechanisms of porosity formation. These mechanisms are illustrated through the example of a 500 particle impact simulation, with no alumina, initial temperature of 412 K and initial speed of 550  $\text{m s}^{-1}$ . Fig. 10 shows the spatial configuration of the particles at the beginning of the simulation.

Two phenomena were identified as principal mechanisms for the formation of porosity during cold spray: surface irregularities and variations of particle local density within the stream.

Surface irregularities occur when a particle impacts an irregular surface. Local topographical features prevent the splat to cover the whole surface at its disposal during its deformation at impact. As a consequence, small pores are created locally at the interface, which will be referred to as interfacial porosity in the following.

Variations of particle local density within the stream lead to stack up flaws. Particles accumulating in a column leave empty spaces on their sides. These defects are closed later by a larger impacting particle, or during further nozzle passes. This mechanism results in the creation of columnar pore, which is generally bigger than the interfacial one. The two mechanisms are illustrated in Figs. 11, 12, 13 and 14. As will be shown in the following, they can interact giving rise to complex pore networks typical of cold spray coatings.

1. Fig. 11,  $t = 150 \text{ ns}$ : at the beginning of the impact of the particle group, a zone with lower particle density can be seen in (a). Some surface irregularities can be seen in the triple cut view (b) around G1, that will lead to splat/splat interface porosity.
2. Fig. 12,  $t = 300 \text{ ns}$ : the low particle density zone is still visible on (a). It leads to the formation of a stack up flaw on the cut view (b), indicated by a white arrow. The large particles G1 and G2 have generated interface defects in their neighbourhood.
3. Fig. 13,  $t = 600 \text{ ns}$ : Particles pile up on the edges of the stack up defect, contributing to its growth.
4. Fig. 14,  $t = 3.6 \text{ } \mu\text{s}$ : at the end of the simulation (a) the stack up flaw has been closed on its top, concluding the formation of a columnar pore, while the coating looks dense on the outside (b). It can also be noted that the columnar pore is connected to some interface porosity, showing the interaction of the two mechanisms illustrated here.

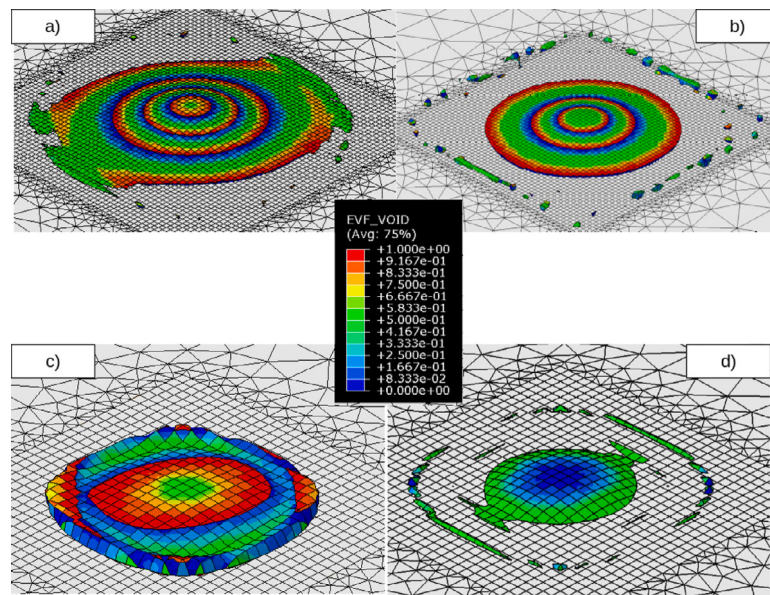


**Fig. 9.** Impact simulations for a single particle of radius 20  $\mu\text{m}$ , with an initial temperature of 573 K. Mesh size and velocity were: (a)  $\text{mf} = 0.1$ ,  $V = 600 \text{ m s}^{-1}$  (b)  $\text{mf} = 0.1$ ,  $V = 700 \text{ m s}^{-1}$  (c)  $\text{mf} = 0.2$ ,  $V = 600 \text{ m s}^{-1}$  (d)  $\text{mf} = 0.2$ ,  $V = 700 \text{ m s}^{-1}$ .

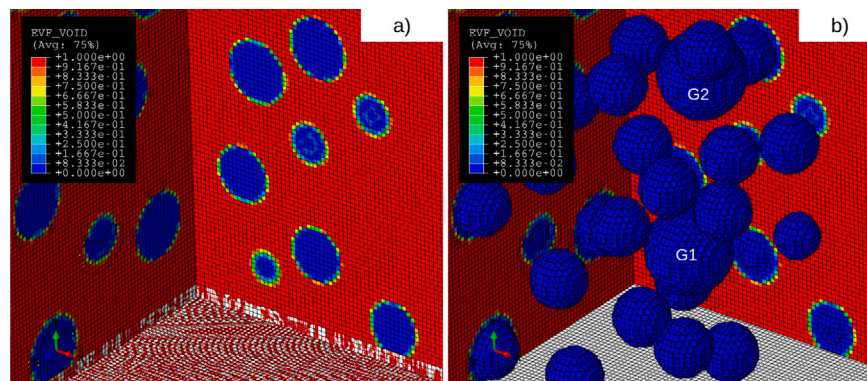


**Fig. 10.** Multi-particle impact simulation at  $t = 0$ , with 500 particles, no alumina, an initial temperature of 412 K and an initial speed of 550  $\text{m s}^{-1}$ . (a) Triple cut view, (b) double cut view. The two labels "G1" and "G2" indicate bigger particles in the population. The colour legend represents the element void fraction. (For interpretation of the references to colour in this figure legend, the reader is referred to the web version of this article.)

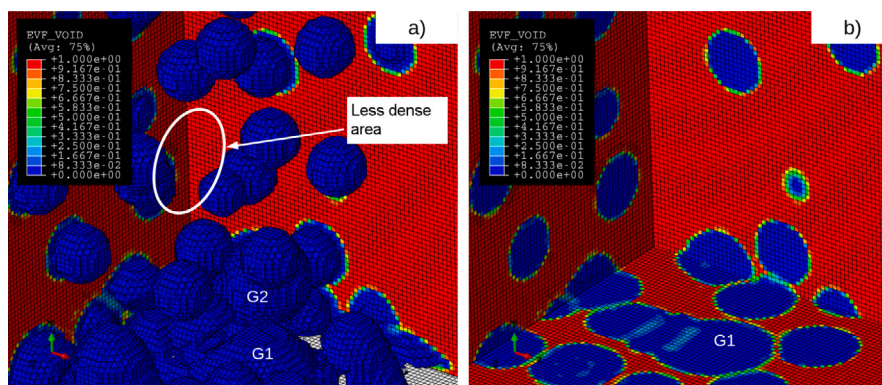


**Fig. 11.**  $t = 150 \text{ ns}$ : (a) double section view, the substrate is visible in grey, below the particles. (b) Triple section view with interface defects. The zone with low particle density is circled in white. (For interpretation of the references to colour in this figure legend, the reader is referred to the web version of this article.)

The mechanism of porosity formation proposed here is based on purely geometrical effects and did not take into account the role of the oxide layer. However, it can be assumed that the oxide layer has a negligible effect at the scale considered for the simulation (*i.e.* particle

size), with elements measuring few micrometres. Oxide layer has been proved to have a significant effect on particle adhesion mechanisms and it can therefore have a role on interface pore formation mechanisms at a smaller scale, typically smaller than 1  $\mu\text{m}$ . This kind of porosity has

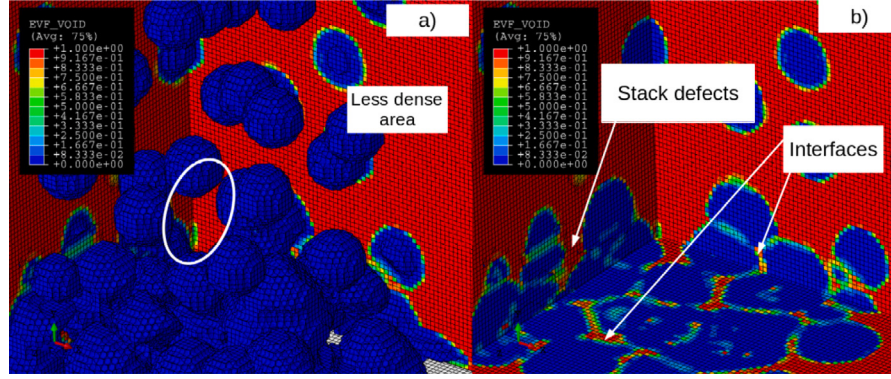


**Fig. 12.**  $t = 300$  ns: (a) double section view, (b) triple section view. The zone with low particle density is circled in white. (For interpretation of the references to colour in this figure legend, the reader is referred to the web version of this article.)

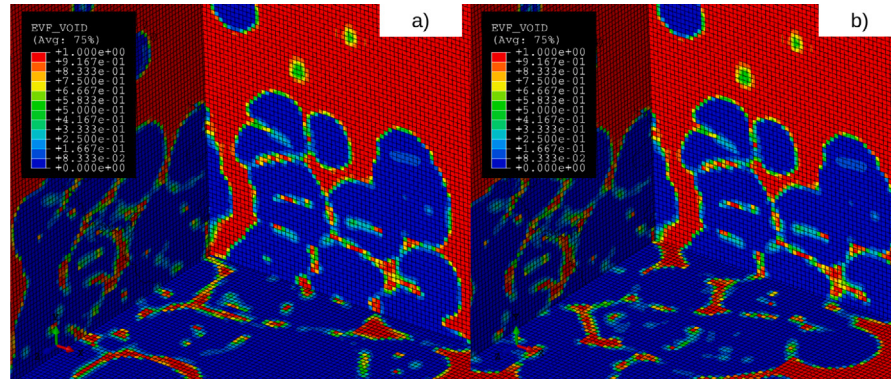


**Fig. 13.**  $t = 600$  ns: (a) triple cut view at altitude A, (b) triple cut view at altitude  $A' > A$ .

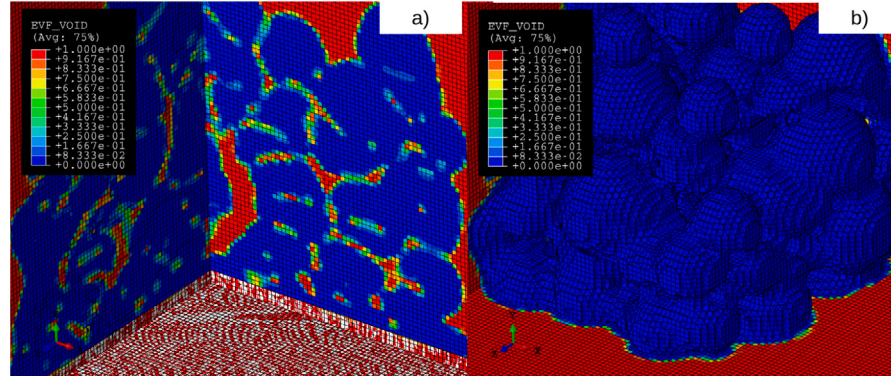


**Fig. 14.**  $t = 3.6 \mu s$ : (a) triple section view, (b) double section view with particles.

been observed by Transmission Electron Microscope in another study by the authors [26]. It will not be discussed further here, being outside of the scope of the present work.

It should be considered that this study highlights mechanisms of porosity formation in a general and qualitative way. The material model chosen does not have a considerable influence on these mechanisms. Differences in particle deformation behaviour produced by a different choice of the material law or model parameters will not drastically modify the mechanisms proposed here, even if can bring to quantitative differences in porosity level estimation.

A more representative distribution of particle size, temperature and initial velocity would also provide a more accurate description of the mechanisms involved in the formation of porosity. However, this would be at the expense of the computational time and power required: a

large number of interacting particles is necessary to describe these mechanisms adequately.

The analysis of multi-particle impact simulations allowed to get insights on the creation of percolating pore. The latter means that a connected path through open porosity exists in the coating. Understanding this feature is crucial for some applications, needing a coating capable of completely isolate the substrate from the external atmosphere (for instance anti-corrosion or gas-tight coatings).

Open porosity is generally connected to the atmosphere by interface flaws, that are the entry points in the coating for potential gas flows or corrosion paths. These interface flaws sometimes open into a columnar pore, which acts as a connector bridge in the coating and allow spatially distant interface pores to be linked. The creation of such a pore network is illustrated in Fig. 15, showing the formation of an interconnected porosity network in a simulated coating.

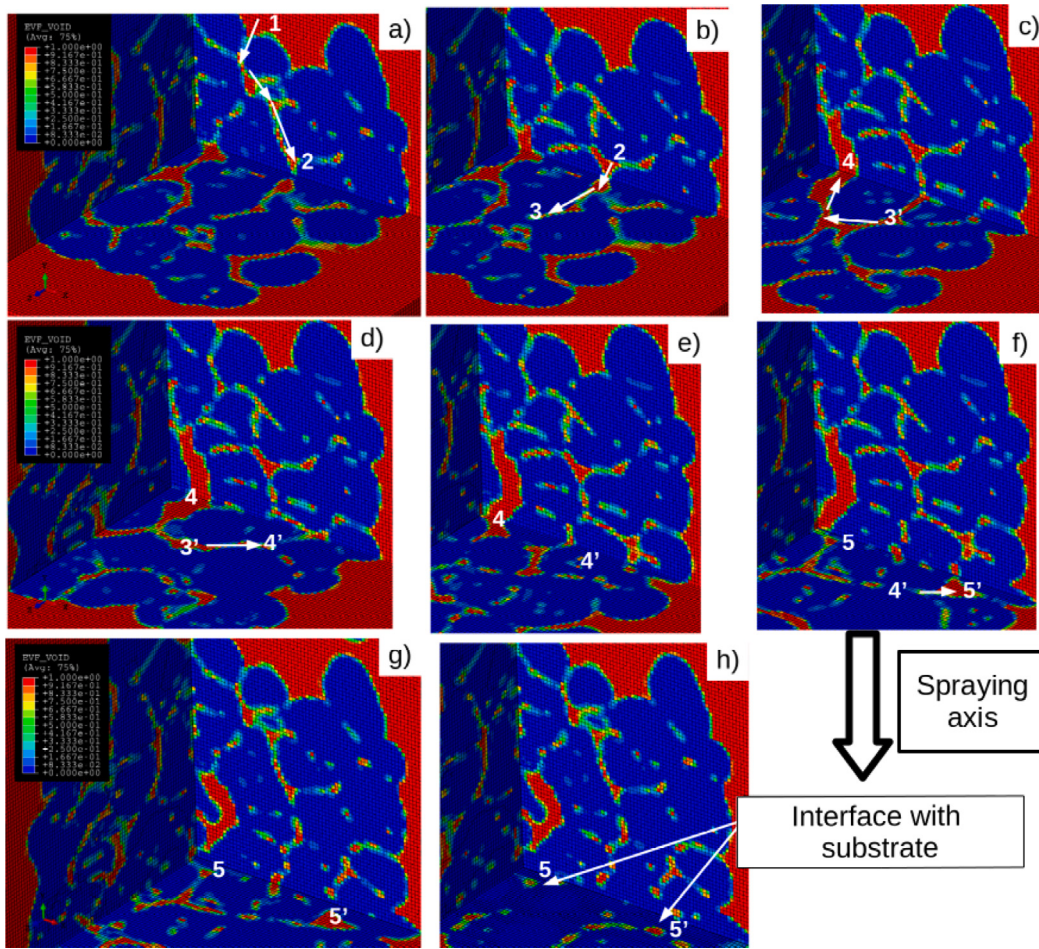


**Fig. 15.** Path of a percolating porosity through the coating, connecting the external environment to the surface of the substrate.

- (a) Interface pores connect point 1 to point 2 along the spraying axis.
- (b) Point 2 is connected to point 3 along the plane perpendicular to the spraying axis.
- (c) Point 3 is connected to point 3' via an interface pore, itself connected to point 4 via a columnar pore.
- (d) The columnar pore acts as a crossroads connecting interface pores. 3' is connected to 4'.
- (e) The points 4 and 4' are connected.
- (f) 4 and 4' are connected to 5 and 5' along the spraying axis.
- (g) and (h) Points 5 and 5' arrive at the coating-substrate interface.

Percolating porosity in cold spray coatings thus seems to arise from the joint action of the two mechanisms proposed in the present work, responsible for the formation of columnar and interface pores.

An experimental observation of a coating elaborated with pure spherical Al powder (shown in Fig. 16) was carried out, in order to assess the mechanisms highlighted by numerical simulation.

Columnar and interface pores can be observed with shapes similar to the ones obtained by numerical simulation. The experimental observation confirms the presence of a pore network percolating along the spraying axis, similar to the one evidenced in the simulations. This tends to confirm the overall mechanisms involved in pore formation.

### 3.2.2. Comparison with XMT

The 1D isentropic model presented in the work of Champagne et al. [34] was used to compute velocity and temperature of impacting

**Table 3**  
Porosity levels for finite elements simulation and XMT experimental observations.

Process parameters	Simulation (%)	XMT (%)
3 MPa 300 °C 20% wt. Al <sub>2</sub> O <sub>3</sub>	15.9	1.15
2.5 MPa 350 °C 20% wt. Al <sub>2</sub> O <sub>3</sub>	15.5	1.78
3 MPa 400 °C 20% wt. Al <sub>2</sub> O <sub>3</sub>	13.3	2.02
3 MPa 300 °C no Al <sub>2</sub> O <sub>3</sub>	19.2	1.71

particles. 100 particles were generated with the algorithm presented in Section 2.1.2, according to the experimental particle size distribution 2.4, and the best compromise mesh factor ( $\frac{1}{6}$ ). It yields that mesh size is 3.33 μm and that each particle speed and temperature is computed depending on its size, and on the gas pressure, and temperature. Four simulations were carried out for the same spatial configuration and confinement box size. Three of them incorporated alumina (15 particles out of 100), with the following gas pressures and temperatures, for the 24TC nozzle geometry: 3 MPa 300 °C, 3 MPa 400 °C and 2.5 MPa 350 °C. The last simulation, considering the 33PBI nozzle, was conducted with 100 aluminium particles and no alumina, taking a pressure/temperature couple of 3 MPa and 300 °C for the gas.

Table 3 shows the porosity levels obtained by simulation and those measured by XMT image analysis [26].

The simulated porosity levels are one order of magnitude higher than those measured by XMT. Several explanations can be made.



**Fig. 16.** Cross sectional view in the XZ plane of a tomographic image of a coating, obtained with a spherical aluminium feed-stock powder cold sprayed at 3 MPa, 300 °C and without alumina mixing. The spraying direction is along -z.

**Table 4**  
Comparison of the volume used to compute porosity for finite element simulations and XMT.

Process parameters	FE volume $\mu\text{m}^3$	XMT volume $\mu\text{m}^3$	Ratio $\frac{V_{XMT}}{V_{FE}}$
3 MPa 300 °C 20% wt. $\text{Al}_2\text{O}_3$	$4.85 \cdot 10^4$	$28.9 \cdot 10^6$	594
2.5 MPa 350 °C 20% wt. $\text{Al}_2\text{O}_3$	$4.87 \cdot 10^4$	$33.3 \cdot 10^6$	687
3 MPa 400 °C 20% wt. $\text{Al}_2\text{O}_3$	$4.83 \cdot 10^4$	$28.6 \cdot 10^6$	593
3 MPa 300 °C no $\text{Al}_2\text{O}_3$	$1.81 \cdot 10^5$	$35.2 \cdot 10^6$	194

#### Small volume or small number of particles.

Although the SCH method allows to take into account a maximum volume by avoiding edge effects for the calculation of the porosity, the latter is several orders of magnitude lower than the one considered in XMT. **Table 4** shows the volumes considered in simulation and in XMT, in  $\mu\text{m}^3$ . It is possible that the considerable differences in sampling volumes for the two cases have a strong impact. Porosity levels should be compared on volumes of comparable size. However, the notion of porosity level no longer makes sense below a certain scale. Thus, the volume generated during simulations should be increased. As a first approximation, assuming that the calculation volume of the porosity is proportional to the number of particles, it would be necessary to simulate impacts of 1000 to 10,000 particles for a decent comparison. In this case, the computational cost would become prohibitive.

#### Hammering effect.

The rebound of alumina particles was not modelled in the present work. In the absence of specific contact conditions in the simulation, alumina particles will not bounce in the CEL formulation. In the experimental observations, as shown by alumina volume fractions in the coating, a large fraction of the alumina particles rebounds [39]. Not adhering particles contribute to densify the coating with hammering effect. It is likely that this effect is not negligible for a correct quantitative estimation of the porosity level in simulations. Due to the low number of particles taken into account in the simulations (100), the coating does not benefit from the cumulative impact of thousands of particles (including aluminium) also contributing to its densification, which occurs in the experimental case.

#### Material behaviour law.

Although the mechanisms of porosity formation identified in this study are not questioned by the choice of the material model, it is possible that the quantitative prediction of porosity is affected by the choice of the material model. This involves the deformation behaviour of the particles at impact. A more detailed study concerning the influence of the material model parameters would be necessary.

#### Mesh size.

In their study, [13] showed that the mesh size has a non-negligible impact on porosity calculation. For a given particle size and spatial distribution, the calculated porosity varies from 24.7% for a mesh size of 5  $\mu\text{m}$  to 3.6% for a mesh size of 1.5  $\mu\text{m}$ .

In the work, the mesh study focused on the convergence of temperature, plastic strain and flattening ratio, in the case of a single-particle impact. The calculation of porosity with the SCH method was not subject to a mesh study. It is possible that the mesh factor determined in the single-impact case is not sufficient for a convergence of the porosity level with the SCH method.

However, it should be noted that even with an optimized mesh size for convergence of the porosity calculation, the calculated porosity levels (including error bars) are 30 to more than 100% away from the experimental values in the work of [13] (Figure 12).

#### Internal pore in the feedstock powder.

Porosity from the powder (especially alumina, being sometimes hollow) not closed during the coating build-up might be an additional source.

#### Conclusion of the comparison with XMT.

The simulation of microstructures representative of cold sprayed materials remains a challenge. Our work is in line with the standards of current modelling in the multi-particle finite element case: use of the CEL method, particles distributed according to experimental grain size, velocities and temperatures computed with a fluid mechanic model [13,23]. Despite the addition of new elements to discuss the relevance of the multi-impact simulation and the calculation of the porosity level (user-independent volume with the SCH method, use of the XMT for comparison of the porosity in 3D), the modelling is still limited by the problems listed above, which prevent a solid validation by the experimental data.

## 4. Conclusions

The present finite element study aimed at highlighting the mechanisms of pore formation in cold spray deposits and at numerically evaluating the effect of particle spatial configuration on porosity. The

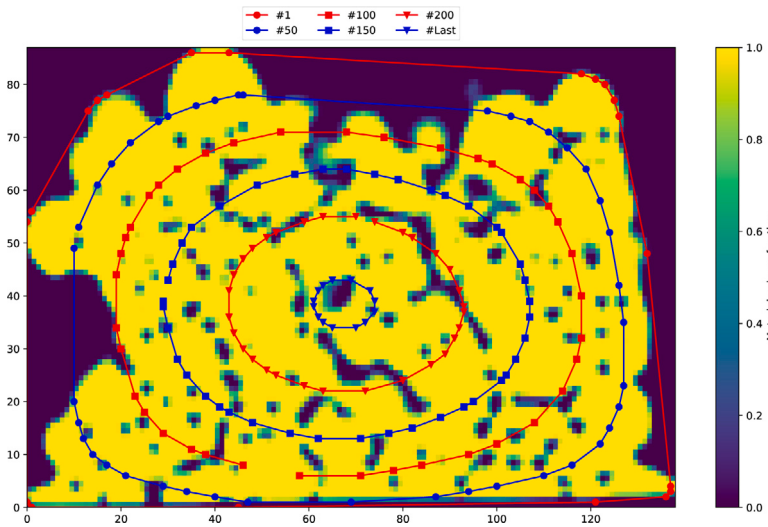


**Fig. C.17.** Cross-sectional view of successive convex envelopes, calculated on a cluster of 500 particles after impact. Spraying direction is from top to bottom of the figure.

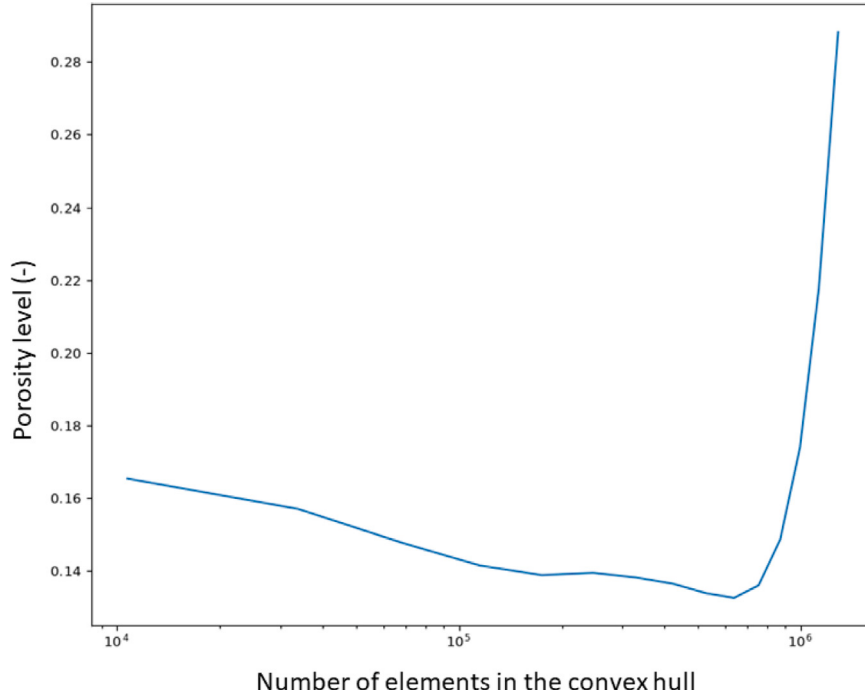


**Fig. C.18.** Pore curve for the simulation with 500 particles,  $T\ 412\ V\ 550\ Al_2O_3\ 0$ .

so-called CEL (Coupled Eulerian Lagrangian) method was used, overcoming the major problems encountered in Lagrangian modelling. The Johnson–Cook material model was chosen, completed by the Mie–Grüneisen equation of state, to account for the behaviour of particles in a fast dynamic regime.

An original method, based on the calculation of successive convex hulls (SCH), was developed to estimate the porosity level in a cluster of deposited particles. The results of 500-particle simulations allowed to propose two mechanisms of porosity formation, while those of 100 particles were sufficient to discuss the influence of the particle spatial configuration on the porosity.

The main mechanisms identified here could rationalize the formation of pore networks in the coating. Interface defects appearing at the particle/particle contact, due to surface irregularities, are combined

with stack up faults, originating from variations in the spatial particle density in the stream. Such stack up defects results in columnar pores, that act as crossroads connecting the interface pores.

It has been shown that the size of the volume in which particles are generated for the simulation, and thus their spatial configuration, has a strong influence on the simulated porosity. A particular attention thus should be paid to this configuration, to avoid biases in numerical studies.

Finally, the comparison in 3D of simulated porosity and experimental observations revealed that the simulation of representative microstructures in cold spray is still a big challenge to be tackled, at least in the case of porosity.

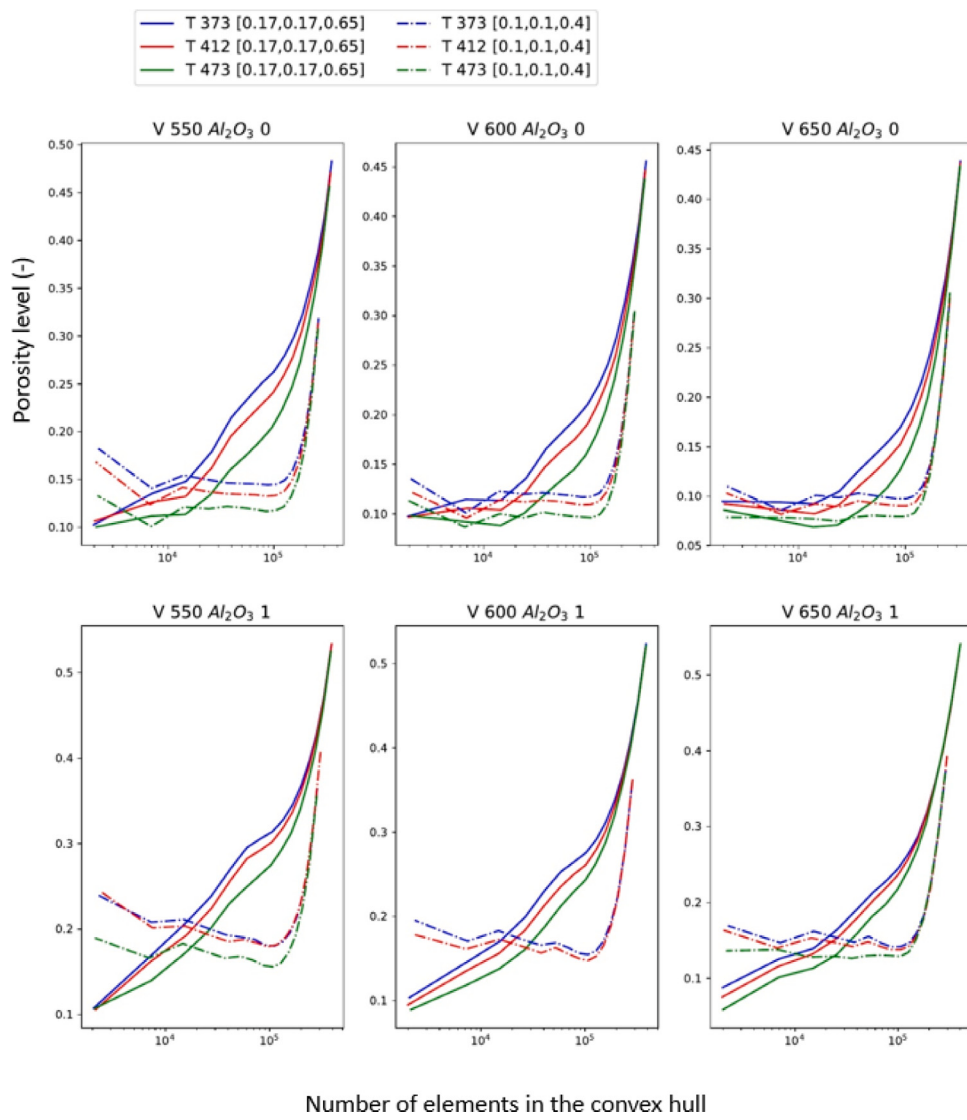


Fig. C.19. Comparisons of the porosity curves for the confinements [0.1, 0.1, 0.4] et [0.17, 0.17, 0.65], for several initial conditions.

#### CRediT authorship contribution statement

**Sebastien Weiller:** Writing – review & editing, Writing – original draft, Validation, Software, Methodology, Investigation, Formal analysis, Conceptualization. **Francesco Delloro:** Writing – review & editing, Validation, Supervision, Conceptualization.

#### Declaration of competing interest

The authors declare that they have no known competing financial interests or personal relationships that could have appeared to influence the work reported in this paper.

#### Data availability

The authors are unable or have chosen not to specify which data has been used.

#### Appendix A. Particles generation algorithm

Given  $N$  the total number of particles to generate:

1. A particle of radius  $R_k$  with its centre expressed in Cartesian coordinates  $C_k$  is randomly generated in the domain, in which  $n$  particles of radii  $R_j$  and centre in Cartesian coordinates  $C_j$ ,  $j \in \llbracket 1, n \rrbracket$  are already present, among the  $N$  to be generated.
2. If the following conditions are satisfied, the particle is generated, otherwise step 1 is repeated.  $D_e$  stands for Euclidean distance.
  - (a) No intersection:  $1.05R_k + \max_{j \in \llbracket 1, n \rrbracket} R_j < \min_{j \in \llbracket 1, n \rrbracket} D_e(C_k, C_j)$ . The 1.05 factor prevents particles from being merged together when meshing.
  - (b) Minimum distance  $m_D$  between particles:  $m_D < \min_{j \in \llbracket 1, n \rrbracket} D_e(C_k, C_j)$ .
  - (c) Maximum distance  $M_D$  between particles:  $\max_{j \in \llbracket 1, n \rrbracket} D_e(C_k, C_j) < M_D$  with  $M_D = n.(D_e(C_k, \sum_{j=1}^n \frac{R_j C_j}{\sum_{k=1}^n R_k}) + R_k + \max_{j \in \llbracket 1, n \rrbracket} R_j)$ .

#### Appendix B. Particles speed and temperature computed with the 1D isentropic model

The following hypothesis and equations are directly taken from [34].

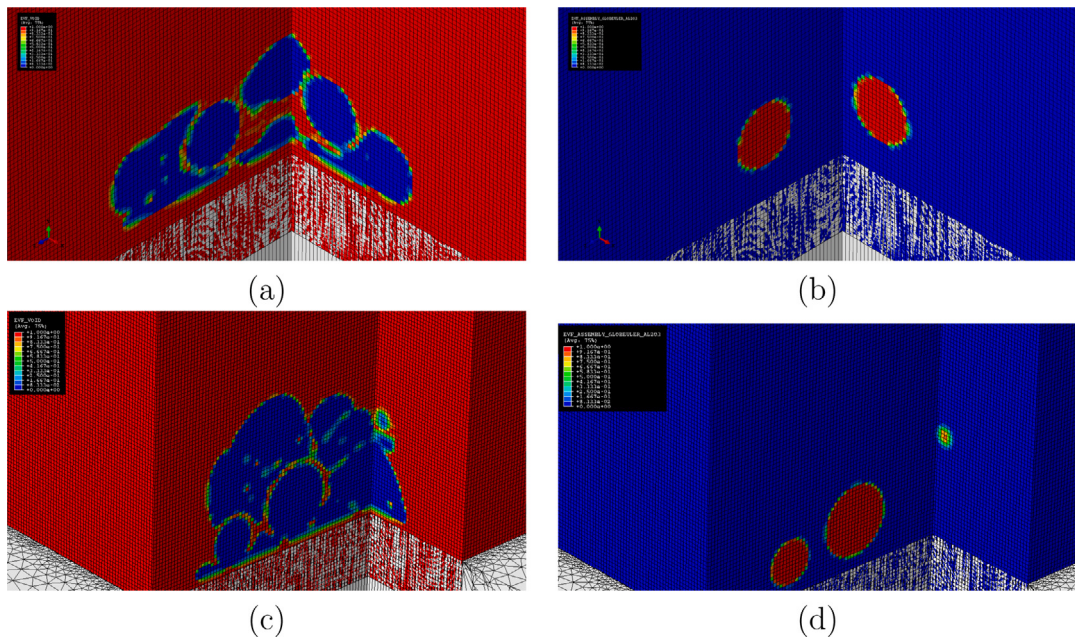


**Fig. C.20.** Final stage of 100-particles impact simulation  $T = 412$  V  $550$   $\text{Al}_2\text{O}_3 = 1$ , with confinement [0.17, 0.17, 0.65] and [0.1, 0.1, 0.4]. Double sections show porosity and phases for [0.17, 0.17, 0.65] in (a) aluminium volume fraction, (b) alumina volume fraction, and for [0.1, 0.1, 0.4] and (c) aluminium volume fraction, (d) alumina volume fraction.

- Gas flow: The gas flow model uses isentropic relationships and linear nozzle geometry. The assumptions for the calculation are as follows:

1. The gas flow is inviscid.
2. The gas flow is adiabatic.
3. The flow velocity, pressure, and density are uniform across any cross section, normal to the nozzle axis.
4. Particles do not influence gas conditions.

This yield the following equation, A being the area of the nozzle at a given location, M the Mach number and  $\gamma$  the ratio of gas specific heats:

$$\frac{A_1}{A_2} = \frac{M_2}{M_1} \left( \frac{1 + 0.5(\gamma - 1)M_1^2}{1 + 0.5(\gamma - 1)M_2^2} \right)^{\frac{\gamma+1}{2(\gamma-1)}} \quad (\text{B.1})$$

- Particle motion is given is computed through the nozzle when gas temperature and velocity through the nozzle is computed, as follow:

$$m \frac{dV_p}{dt} = C_d \frac{\pi}{8} \rho_g d^2 (V_g - V_p)^2 \quad (\text{B.2})$$

where  $m$  is the particle mass,  $V_p$  is the particle velocity,  $C_d$  the drag coefficient,  $\rho_g$  the gas density,  $d$  the particle diameter, and  $V_g$  the gas velocity.

## Appendix C. Complements on the SCH method

### C.1. Computing porosity with the SCH method

For each simulation, after a set of successive convex hulls (SCH)  $E_{c,A_i}$  was obtained, pore volume fraction was calculated on each convex hull of the set. Fig. C.17 illustrates, as an example, the SCH for a simulation of 500 particles. It can be seen that, on one hand, bigger convex hulls contained some of the external void, which would bias the estimation of pore volume fraction. On the other hand, smaller convex hulls contained a small number of pores, with the risk of not being representative of the actual coating porosity. A compromise has to be found between these two opposite trends. To do that, let us analyse

the porosity curve in Fig. C.18, showing pore volume fraction for each successive convex hull. The curve descends monotonically down to a minimum, after which two possible cases can occur:

- the calculation volume becomes smaller and smaller, and the porosity level goes up, as in the present example;
- porosity reaches a plateau and then slightly increases.

In both cases, the first local minimum is taken as the best pore volume fraction estimation. The main advantages of this porosity computational method are: firstly, the choice of the volume does not depend on the user; secondly, the sampling volume is as big as possible, thus being representative of the overall porosity of the particle cluster. The method presents nevertheless some risks: in some cases, the curve decreases monotonically for the whole SCH, or stabilizes at a plateau with a very high value (more than 30%). Unwanted porosity or edge effects then come into consideration and are captured in the envelopes. This can happen when the particles are too far apart at the initial state of the simulation. It is also possible that the total number of particles is too low, in which case the final cluster is excessively spread out in each direction. These unfavourable cases are however originated from an inconvenient simulation set-up and are not linked to a particular weakness of the SCH method. In these unfavourable cases, on the contrary, the SCH method can be an indicator that the calculation of a porosity level is not really relevant and that the simulation set up should be revised.

### C.2. Influence of the confinement box size on the SCH method

In this section, the effect on the SCH method of particle positions at the initial state of the simulation is assessed, as well as the need of carefully choosing the initial volume size in which particles are generated (i.e. the confinement box size). Two particle configurations were generated, differing only for the size of the confinement box (respectively [0.17, 0.17, 0.65] and [0.1, 0.1, 0.4]). The SCH method was then applied and porosity curves will finally be compared, illustrating the effect of the confinement box size on the porosity level.

The simulations were run with the following values for particle temperature and speed:  $T \in \{373, 412, 473\}$  (K),  $V \in \{550, 600, 650\}$  ( $\text{m s}^{-1}$ ) and  $\text{Al}_2\text{O}_3 \in \{0, 1\}$  are presented in Fig. C.19. The results data

for  $T = 473$  V 600  $\text{Al}_2\text{O}_3$  1 with confinement [0.1, 0.1, 0.4] could not be recovered, but this does not change the general trend. The porosity curves for the [0.1, 0.1, 0.4] confinement all show a local minimum and are below those for the [0.17, 0.17, 0.65] confinement. This means that the size of the confinement box in which the particles are generated does have a strong influence on porosity level computation.

Fig. C.20 shows the final stage of the simulation (*i.e.* when particle deformation is accomplished) in double section views at different locations of the coating, for the two confinements [0.17, 0.17, 0.65] (a and b) and [0.1, 0.1, 0.4] (c and d), respectively.

Alumina particles are very poorly embedded in the [0.17, 0.17, 0.65] case, due to lack of hammering and impacting of particles. This creates large voids in the middle of the microstructure. Those voids are taken into account by the convex envelope method, which explains why the porosity curves for [0.17, 0.17, 0.65] are above the ones for [0.1, 0.1, 0.4]. The more strongly the particles are constrained in the plane transverse to the projection axis, the better it is to compute porosity with the SCH method, and presumably with any user-independent porosity computation method.

## References

- [1] J. Villafuerte, *Modern Cold Spray*, Springer International Publishing, Cham, Switzerland, 2015, <http://dx.doi.org/10.1007/978-3-319-16772-5>.
- [2] M. Hassani-Gangaraj, D. Veysset, V.K. Champagne, K.A. Nelson, C.A. Schuh, Response to comment on “adiabatic shear instability is not necessary for adhesion in cold spray”, *Scr. Mater.* 162 (2019) 515–519, <http://dx.doi.org/10.1016/j.scriptamat.2018.12.015>.
- [3] L.L. Koithara, R.N. Raolison, S. Costil, X. Xie, High deposition efficiency and delamination issues during high-pressure cold spraying metallization of PEEK using spherical copper powders, *Int. J. Adv. Manuf. Technol.* 107 (11) (2020) 4427–4436, <http://dx.doi.org/10.1007/s00170-020-05349-z>.
- [4] W. Li, D. Zhang, C. Huang, S. Yin, M. Yu, F. Wang, H. Liao, Modelling of impact behaviour of cold spray particles: Review, *Surf. Eng.* 30 (5) (2014) 299–308, <http://dx.doi.org/10.1179/1743294414Y.0000000268>.
- [5] P.-E. Leger, *Rôle de la microstructure sur les mécanismes de corrosion marine d'un dépôt à base d'aluminium élaboré par projection dynamique par gaz froid (cold spray)* (Ph.D. thesis), Mines ParisTech, 2018.
- [6] T. Schmidt, F. Gärtner, H. Assadi, H. Kreye, Development of a generalized parameter window for cold spray deposition, *Acta Mater.* 54 (3) (2006) 729–742, <http://dx.doi.org/10.1016/j.actamat.2005.10.005>.
- [7] K. Kim, W. Li, X. Guo, Detection of oxygen at the interface and its effect on strain, stress, and temperature at the interface between cold sprayed aluminum and steel substrate, *Appl. Surf. Sci.* 357 (2015) 1720–1726, <http://dx.doi.org/10.1016/j.apsusc.2015.10.022>.
- [8] V. Lemiale, P.C. King, M. Rudman, M. Prakash, P.W. Cleary, M.Z. Jahedi, S. Gulizia, Temperature and strain rate effects in cold spray investigated by smoothed particle hydrodynamics, *Surf. Coat. Technol.* 254 (2014) 121–130, <http://dx.doi.org/10.1016/j.surfcoat.2014.05.071>.
- [9] F. Delloro, M. Jeandin, D. Jeulin, H. Proudhon, M. Faessl, L. Bianchi, E. Meillot, L. Helfen, A morphological approach to the modeling of the cold spray process, *J. Therm. Spray Technol.* 26 (8) (2017) 1838–1850, <http://dx.doi.org/10.1007/s11666-017-0624-8>.
- [10] W.-Y. Li, W. Gao, Some aspects on 3D numerical modeling of high velocity impact of particles in cold spraying by explicit finite element analysis, *Appl. Surf. Sci.* 255 (18) (2009) 7878–7892, <http://dx.doi.org/10.1016/j.apsusc.2009.04.135>, URL: <https://www.sciencedirect.com/science/article/pii/S0169433209005170>.
- [11] S. Rahmati, B. Jodoin, Physically based finite element modeling method to predict metallic bonding in cold spray, *J. Therm. Spray Technol.* 29 (4) (2020) 611–629, <http://dx.doi.org/10.1007/s11666-020-01000-1>.
- [12] W. Li, K. Yang, S. Yin, X. Guo, Numerical analysis of cold spray particles impacting behavior by the eulerian method: a review, *J. Therm. Spray Technol.* (2016) <http://dx.doi.org/10.1007/s11666-016-0443-3>.
- [13] X. Song, K.L. Ng, J.M.-K. Chea, W. Sun, A.W.-Y. Tan, W. Zhai, F. Li, I. Marinescu, E. Liu, Coupled Eulerian-Lagrangian (CEL) simulation of multiple particle impact during Metal Cold Spray process for coating porosity prediction, *Surf. Coat. Technol.* 385 (2020) 125433, <http://dx.doi.org/10.1016/j.surfcoat.2020.125433>.
- [14] J. Xie, Simulation of Cold Spray Particle Deposition Process, Lyon, INSA, 2014, URL: <http://www.theses.fr/2014ISAL0044>.
- [15] B. Gnanasekaran, G.-R. Liu, Y. Fu, G. Wang, W. Niu, T. Lin, A Smoothed Particle Hydrodynamics (SPH) procedure for simulating cold spray process - A study using particles, *Surf. Coat. Technol.* 377 (2019) 124812, <http://dx.doi.org/10.1016/j.surfcoat.2019.07.036>.
- [16] A. Moridi, S.M. Hassani-Gangaraj, M. Guagliano, A hybrid approach to determine critical and erosion velocities in the cold spray process, *Appl. Surf. Sci.* 273 (2013) 617–624, <http://dx.doi.org/10.1016/j.apsusc.2013.02.089>.
- [17] J. Xie, D. Nelias, H. Berre, K. Ogawa, Y. Ichikawa, Simulation of the cold spray particle deposition process, *J. Tribol.* 137 (4) (2015) 041101, <http://dx.doi.org/10.1115/1.4030257>.
- [18] A. Fardan, C.C. Berndt, R. Ahmed, Numerical modelling of particle impact and residual stresses in cold sprayed coatings: A review, *Surf. Coat. Technol.* 409 (2021) 126835, <http://dx.doi.org/10.1016/j.surfcoat.2021.126835>.
- [19] G. Boletti, S. Dosta, L. Lusvarghi, T. Manfredini, J. Guilemany, I. Cano, Building up WC-Co coatings by cold spray: A finite element simulation, *Surf. Coat. Technol.* 374 (2019) 674–689, <http://dx.doi.org/10.1016/j.surfcoat.2019.06.054>.
- [20] C. Chen, Y. Xie, C. Verdy, R. Huang, H. Liao, Z. Ren, S. Deng, Numerical investigation of transient coating build-up and heat transfer in cold spray, *Surf. Coat. Technol.* 326 (2017) 355–365, <http://dx.doi.org/10.1016/j.surfcoat.2017.07.069>.
- [21] H. Wu, X. Xie, M. Liu, C. Chen, H. Liao, Y. Zhang, S. Deng, A new approach to simulate coating thickness in cold spray, *Surf. Coat. Technol.* 382 (2020) 125151, <http://dx.doi.org/10.1016/j.surfcoat.2020.125151>.
- [22] S. Msolli, Z.-Q. Zhang, D.H.L. Seng, Z. Zhang, J. Guo, C. Reddy, N. Sridhar, J. Pan, B.H. Tan, Q. Loi, An experimentally validated dislocation density based computational framework for predicting microstructural evolution in cold spray process, *Int. J. Solids Struct.* 225 (2021) 111065, <http://dx.doi.org/10.1016/j.ijsolstr.2021.111065>.
- [23] M. Terrone, A.A. Lordejani, J. Kondas, S. Bagherifard, A numerical Approach to design and develop freestanding porous structures through cold spray multi-material deposition, *Surf. Coat. Technol.* 421 (2021) 127423, <http://dx.doi.org/10.1016/j.surfcoat.2021.127423>.
- [24] S.H. Zahiri, D. Fraser, S. Gulizia, M. Jahedi, Effect of processing conditions on porosity formation in cold gas dynamic spraying of copper, *J. Therm. Spray Technol.* 15 (3) (2006) 422–430, <http://dx.doi.org/10.1361/105996306X124437>.
- [25] Y. Wang, J. Adrien, B. Normand, Porosity characterization of cold sprayed stainless steel coating using three-dimensional X-ray microtomography, *Coatings* 8 (9) (2018) 326, <http://dx.doi.org/10.3390/coatings8090326>.
- [26] S. Weiller, F. Delloro, F. Willot, A. Thorel, M. Jeandin, C. Garion, Influence of porosity on ultra-high vacuum gas-tightness in cold-sprayed aluminum coatings, *Transp. Porous Media* (2022) <http://dx.doi.org/10.1007/s11242-022-01806-3>.
- [27] G. Johnson, W. Cook, A constitutive model and data for metals subjected to large strains, high strain rates, and high temperatures, 1983.
- [28] D.S. Lemons, C.M. Lund, Thermodynamics of high temperature, Mie–Gruneisen solids, *Amer. J. Phys.* 67 (12) (1999) 1105, <http://dx.doi.org/10.1119/1.19091>.
- [29] Q. Wang, N. Ma, M. Takahashi, X. Luo, C. Li, Development of a material model for predicting extreme deformation and grain refinement during cold spraying, *Acta Mater.* 199 (2020) 326–339, <http://dx.doi.org/10.1016/j.actamat.2020.08.052>.
- [30] M.C. Price, A.T. Kearsley, M.J. Burchell, Validation of the [preston-tonks-wallace] strength model at strain rates approaching ~1011 s<sup>-1</sup> for Al-1100, tantalum and copper using hypervelocity impact crater morphologies, *Int. J. Impact Eng.* 52 (2013) 1–10, <http://dx.doi.org/10.1016/j.ijimpeng.2012.09.001>.
- [31] G.R. Johnson, Material characterization for warhead computations, *Progr. Astronaut. Aeronaut.* 155 (1993) 165.
- [32] A. Hor, Simulation physique des conditions thermomécaniques de forgeage et d'usinage: caractérisation et modélisation de la rhéologie et de l'endommagement (Ph.D. thesis), Arts et Métiers ParisTech, French, 2011, p. 78, table 3.4, URL: <https://tel.archives-ouvertes.fr/pastel-00593068>.
- [33] M. Arrigoni, M. Boustie, C. Bolis, S. Barradas, L. Berthe, M. Jeandin, Shock mechanics and interfaces, in: *Mechanics of Solid Interfaces*, John Wiley & Sons, Ltd, 2012, pp. 211–248, <http://dx.doi.org/10.1002/9781118561669.ch7>.
- [34] V.K. Champagne, D.J. Helfritch, S.P.G. Dinavahi, P.F. Leyman, Theoretical and experimental particle velocity in cold spray, *J. Therm. Spray Technol.* 20 (3) (2011) 425–431, <http://dx.doi.org/10.1007/s11666-010-9530-z>.
- [35] P.C. King, S. Zahiri, M. Jahedi, J. Friend, Aluminium coating of lead zirconate titanate—A study of cold spray variables, *Surf. Coat. Technol.* 205 (7) (2010) 2016–2022, <http://dx.doi.org/10.1016/j.surfcoat.2010.08.084>.
- [36] T.M. Chan, Optimal output-sensitive convex hull algorithms in two and three dimensions, *Discrete Comput. Geom.* 16 (4) (1996) 361–368, <http://dx.doi.org/10.1007/BF02712873>.
- [37] M. Faessl, licence simple morphological image library, 2019, URL: <http://smil.cmm.mines-paristech.fr/wiki/doku.php/licence>.
- [38] M. Hassani, D. Veysset, C. Victor Jr., K. Nelson, C. Schuh, Adiabatic shear instability is not necessary for adhesion in cold spray, *Acta Mater.* 158 (2018) <http://dx.doi.org/10.1016/j.actamat.2018.07.065>.
- [39] R. Fernandez, B. Jodoin, Cold spray aluminum - alumina cermet coatings: effect of alumina content, *J. Therm. Spray Technol.* 27 (4) (2018) 603–623, <http://dx.doi.org/10.1007/s11666-018-0702-6>.